MATHEMATICAL BIOSCIENCES
AND ENGINEERING
Volume **13**, Number **1**, February **2016**

doi:10.3934/mbe.2016.13.43

pp. **43–65**

MODELLING THE SPATIAL-TEMPORAL PROGRESSION OF THE 2009 A/H1N1 INFLUENZA PANDEMIC IN CHILE

Raimund Bürger

CI^{2}MA and Departamento de Ingeniería Matemática, Universidad de Concepción
Casilla 160-C, Concepción, Chile

Gerardo Chowell

School of Public Health, Georgia State University
Atlanta, Georgia, USA
and
Simon A. Levin Mathematical and Computational Modeling Sciences Center
School of Human Evolution and Social Change, Arizona State University
Tempe, AZ 85287, USA
and
Division of International Epidemiology and Population Studies
Fogarty International Center, National Institutes of Health
Bethesda, MD 20892, USA

Pep Mulet

Departament de Matemàtica Aplicada, Universitat de València
Av. Dr. Moliner 50, E-46100 Burjassot, Spain

Luis M. Villada

GIMNAP-Departamento de Matemáticas, Universidad del Bío-Bío
Casilla 5-C, Concepción, Chile
and
CI^{2}MA, Universidad de Concepción
Casilla 160-C, Concepción, Chile

(Communicated by Christopher M. Kribs)

Abstract. A spatial-temporal transmission model of 2009 A/H1N1 pandemic influenza across Chile, a country that spans a large latitudinal range, is developed to characterize the spatial variation in peak timing of that pandemic as a function of local transmission rates, spatial connectivity assumptions for Chilean regions, and the putative location of introduction of the novel virus into the country. Specifically, a metapopulation SEIR (susceptible-exposed-infected-removed) compartmental model that tracks the transmission dynamics of influenza in 15 Chilean regions is calibrated. The model incorporates population mobility among neighboring regions and indirect mobility to and from other regions via the metropolitan central region ("hub region"). The stability of the disease-free equilibrium of this model is analyzed and compared with the corresponding stability in each region, concluding that stability may occur even with some regions having basic reproduction numbers above 1. The transmission model is used along with epidemiological data to explore

2010 *Mathematics Subject Classification.* Primary: 92D30; Secondary: 97M60.

Key words and phrases. Spatial-temporal SEIR model, pandemic, metapopulation model, stability of disease-free equilibrium.

potential factors that could have driven the spatial-temporal progression of the pandemic. Simulations and sensitivity analyses indicate that this relatively simple model is sufficient to characterize the south-north gradient in peak timing observed during the pandemic, and suggest that south Chile observed the initial spread of the pandemic virus, which is in line with a retrospective epidemiological study. The "hub region" in our model significantly enhanced population mixing in a short time scale.

1. **Introduction.**

1.1. **Spatial-temporal variation of influenza.** Increasing our understanding of the spatial dissemination patterns of influenza is essential for public health surveillance and the implementation of reactive social distancing measures for mitigation efforts. Factors that have been associated with the spatial-temporal variation in seasonal influenza activity at the city or regional level include local environmental characteristics (e.g., temperature, specific humidity [44, 48] that enable local transmission, school cycles [9, 26] whereby influenza transmission rates tend to decline during school breaks, as well as regional and global population mobility patterns [7, 15, 49]). For instance, a study based on 30 years of influenza-related mortality found a significant correlation between influenza activity across U.S. states and the rates of movement of people to and from their workplaces (workflows) compared with geographical distance [49]. Another study using influenza hospitalization records among older adult populations across U.S. states found a significant gradient in the peak timing of influenza at the state level whereby western states tended to peak earlier than northeastern states [51]. Similarly, another study based on weekly laboratory-confirmed influenza A from Canadian and U.S. influenza surveillance systems showed a slight gradient in peak timing from the southwest regions in the U.S. to northeast regions of Canada and the U.S. This study also found that regional influenza epidemics were more synchronized across the U.S. (3–5 weeks) compared with Canada (5–13 weeks) [41].

1.2. **The 2009 A/H1N1 pandemic influenza in Chile.** In the context of the recent 2009 A/H1N1 influenza pandemic, population contact rates linked to school cycles or intervention strategies [11, 13, 23, 52], demographic factors [36], local transmissibility [11–13], and global mobility patterns, driving the timing of introduction of the virus across countries [29], have been associated with the complex spatial and temporal evolution of the 2009 A/H1N1 influenza pandemic. The 2009 A/H1N1 influenza pandemic spread across Chile during the winter months of 2009 soon after the first cases had been confirmed in Mexico and California, USA [37]. The first two cases of novel 2009A/H1N1 influenza in Chile were confirmed in metropolitan Santiago on May 17, 2009 [37]. However, a retrospective study based on emergency room visit and laboratory viral surveillance conducted in the southern city of Puerto Montt, capital of Los Lagos region, suggested that this city could have experienced both earlier pandemic onset and a faster transmission rate compared to the metropolitan area of Santiago [37]. Indeed, an analysis of epidemiological data of the 2009 A/H1N1 influenza pandemic in Chile showed that this country experienced a latitudinal gradient in pandemic peak timing in 2009, with southern regions experiencing earlier pandemic activity compared to northern regions [12] (Figure 1 (b)). Specifically, the southernmost regions (Biobío, Araucanía, Los Ríos, Los Lagos, Aysén, and Magallanes) exhibited an early A/H1N1 pandemic peak, occurring about 16–39 days earlier relative to the northernmost Chilean region (Arica y Parinacota). The same study found that this geographical variation in pandemic

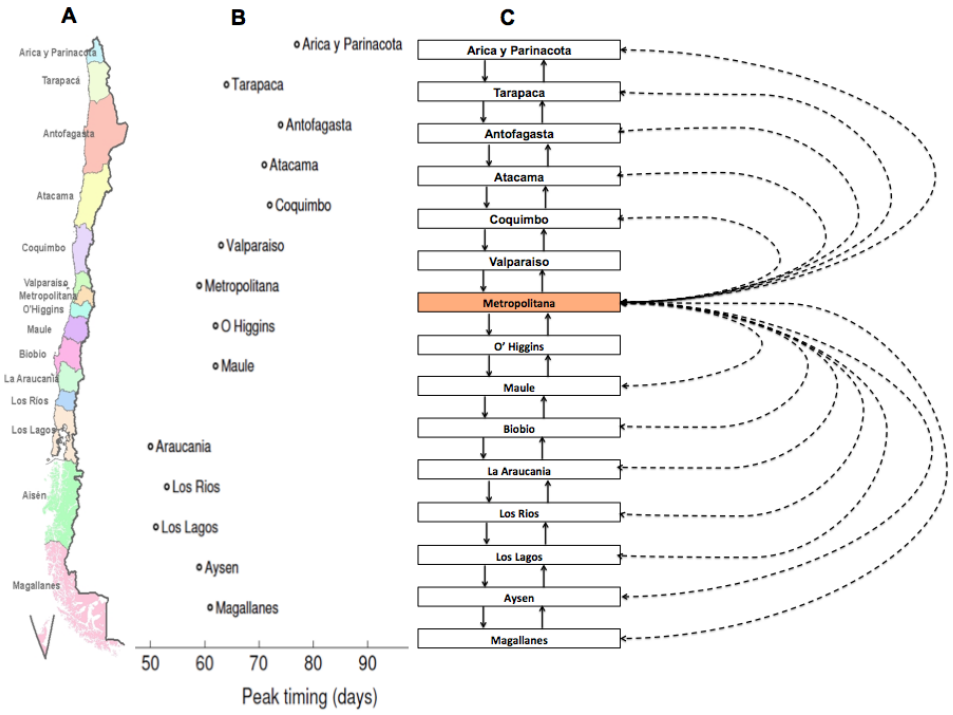

FIGURE 1. (a) Chile comprises 15 regions that follow a north-south pattern spanning a large latitudinal gradient. (b) The 2009 A/H1N1 influenza pandemic peak timing across the 15 Chilean regions relative to May 1st 2009 shows a significant gradient in pandemic peak timing, with southern regions experiencing earlier pandemic activity compared to northern regions. (c) Schematic representation of population's mobility patterns incorporated in our metapopulation model comprising 15 Chilean regions from north to south of Chile. Arrows indicate that individuals in each region are allowed to move to and from neighboring regions as well as the metropolitan region ("hub") located in central Chile.

peak timing in Chile was significantly associated with differences in latitude and climatic conditions, with latitude, maximum temperature and specific humidity accounting for 69–80% of this variability in pandemic peak timing [12]. In fact, this south-north gradient in pandemic peak timing reported for Chile is consistent with a decreasing trend in transmissibility in the same direction, which was found to be statistically associated with maximum temperature and specific humidity. This is also consistent with experimental studies suggesting that influenza transmission is more efficient under dry and cold conditions [33–35, 43, 44, 46].

1.3. **This contribution.** Here we develop a spatial-temporal transmission model of 2009 A/H1N1 pandemic influenza. We tailor this model to the pandemic progression in Chile, a country that spans a large latitudinal gradient, in order to characterize the spatial variation in pandemic peak timing of influenza in terms of local transmission rates, spatial connectivity assumptions across Chilean regions

Region		population	Region		population
1	Arica y Parinacota	213816	9	Maule	968336
2	Tarapacá	300021	10	Biobío	1971998
3	Antofagasta	547463	11	Araucanía	913065
4	Atacama	292054	12	Los Ríos	364592
5	Coquimbo	707654	13	Los Lagos	798141
6	Valparaíso	1734917	14	Aysén	99609
7	Metropolitana	6685685	15	Magallanes	159468
8	O'Higgins	877784	Chile (total)		16634603

TABLE 1. Official data for population (2009) [25]. Note that we number regions consecutively from north to south; our numbering does not coincide with the official governmental numbers of regions.

and the putative location of introduction of the virus into the country. More specifically, we employ epidemic modeling together with epidemiological data to explore the spatial-temporal progression of pandemic influenza in Chile by testing a range of transmission scenarios to investigate the robustness of the south-north gradient observed during the 2009 influenza pandemic in Chile. We analyze the relationship between the stability of the Disease-Free Equilibrium (DFE) for the model and the stability of the local DFE in each region, to arrive at the conclusion that local stability implies global stability, but the reciprocal implication does not necessary hold, by providing a counterexample for which the DFE is stable whereas the basic reproduction number at some region is above 1.

2. **Spatial-temporal SEIR model.** Classical SEIR (susceptible-exposed-infectious-recovered) epidemiological models describe disease transmission in homogeneous populations by classifying individuals into one of four different epidemiological states [3,8,16,18,28,39,50]. However, these single-population models rely on the strong assumption that the entire population is mixing homogeneously (e.g., each individual in the population has the same probability of contacting any other individual in the population). Hence, these models do no consider any aspects about the spatial spread of the disease across large geographic areas which could differ in demographic, environmental, and other characteristics that could influence disease transmission.

2.1. **Formulation of the SEIR transmission model.** We employ a SEIR transmission model with $n = 15$ contiguous populations sorted from north to south Chile (Figure 1 (a) and Table 1) according to the 15 administrative regions. We model two types of population mobility: 1) movement to and from adjacent regions and 2) long-distance population mixing via the central metropolitan ("hub") region that is connected to all regions (see Figure 1 (c)). Therefore, region 1 corresponds to the northernmost region, region n is the southernmost region, and region j_0 denotes the metropolitan ("hub") region. The metropolitan region in Chile (the greater Santiago area) comprises the main airport and several bus terminals. Virtually all trips by bus or air between northern and southern regions involve a stopover in the hub region, as do many flight connections whose origin and destination are both located either north or south of the hub region, e.g. travelling between the Biobío and Magallanes regions usually is via the hub region.

We keep track of the numbers of susceptible, exposed, infectious and recovered individuals in each of the 15 Chilean regions at time t, denoted by $S_j(t)$, $E_j(t)$,

$I_j(t)$ and $R_j(t)$ for $j = 1, \dots, n$, respectively, via dynamic equations. Moreover, we do not model disease-induced deaths as the 2009 A/H1N1 influenza pandemic generated very low mortality rates in most areas of the world including Chile, our population of interest. In fact, the A/H1N1 pandemic mortality rate for Chile has been estimated at 2 deaths per 100,000 people [45].

The disease transmission is described by the following system of $4n$ ordinary differential equations, where the total population size in each region j is given by $N_j(t) = S_j(t) + E_j(t) + I_j(t) + R_j(t)$:

$$\begin{aligned} \frac{\mathrm{d}S_j}{\mathrm{d}t} &= -\beta_j \frac{S_j I_j}{N_j} + \mathcal{M}_j(S), & \frac{\mathrm{d}I_j}{\mathrm{d}t} &= \kappa E_j - \gamma I_j + \mathcal{M}_j(I), \\ \frac{\mathrm{d}E_j}{\mathrm{d}t} &= \beta_j \frac{S_j I_j}{N_j} - \kappa E_j + \mathcal{M}_j(E), & \frac{\mathrm{d}R_j}{\mathrm{d}t} &= \gamma I_j + \mathcal{M}_j(R) \quad \text{for } j = 1, \dots, n. \end{aligned} \tag{1}$$

The local transmission rate in each region j is given by a constant β_j, where we model an increasing transmissibility gradient from north to south Chile (as previously reported in [12]) by assuming that

$$\beta_1 < \beta_2 < \cdots < \beta_n. \tag{2}$$

Moreover, as usual, $1/\kappa$ is the latent period, $1/\gamma$ is the infectious period and $\mathcal{M}_j(X)$ for $X \in \{S, E, I, R\}$ is the movement operator in region j. The mobility of individuals in our model is governed by the following rules:

- Nearest-neighbor mobility for all regions $j = 1, \dots, n$. Individuals in region j are allowed to move to regions $j-1$ and $j+1$ at respective rates $\hat{m}_{j-1,j}$ and $\hat{m}_{j+1,j}$ except that individuals in the northernmost region 1 can only move to region 2, and similarly, individuals in the southernmost region n can only move to region $n-1$ (see Figure 1 (c)). Here we assume that $\hat{m}_{j-1,j} = \hat{m}_{j,j-1} =: m_{j-1/2}$.
- We also consider long-range movement to the rest of the country via a "hub region" denoted by index j_0 that corresponds to the metropolitan region in central Chile (Figure 1 (c)). That is, individuals in region j move to region j_0 (the "hub region") at rate $m_{\mathrm{h},j}$ for $j = 1, \dots, n$, and similarly individuals in j_0 move to other regions at the same rate $m_{\mathrm{h},j}$.

The above assumptions regarding population mobility lead to the following explicit definition of the operator $\mathcal{M}_j(X)$ for $j = 1, \dots, n$:

$$\mathcal{M}_j(X) = \begin{cases} m_{3/2}X_2 + m_{\mathrm{h},1}X_{j_0} - (m_{3/2} + m_{\mathrm{h},1})X_1 & \text{for } j = 1, \\ m_{j_0-1/2}X_{j_0-1} + m_{j_0+1/2}X_{j_0+1} + \sum_{i=1}^n m_{\mathrm{h},i}X_i & \\ \quad -(m_{j_0-1/2} + m_{j_0+1/2} + \sum_{i=1}^n m_{\mathrm{h},i})X_{j_0} & \text{for } j = j_0, \\ m_{n-1/2}X_{n-1} + m_{\mathrm{h},n}X_{j_0} - (m_{n-1/2} + m_{\mathrm{h},n})X_n & \text{for } j = n, \\ m_{j-1/2}X_{j-1} + m_{j+1/2}X_{j+1} + m_{\mathrm{h},j}X_{j_0} & \\ \quad -(m_{j-1/2}X_{j-1} + m_{j+1/2}X_{j+1} + m_{\mathrm{h},j})X_j & \text{otherwise.} \end{cases}$$

The matrix $\boldsymbol{M} = (m_{ij})_{1 \le i,j \le n}$ such that $\mathcal{M}_j(X) = (\boldsymbol{M}(X_1, \dots, X_n)^{\mathrm{T}})_j$ is given by

$$\boldsymbol{M} = -\boldsymbol{\Delta} - \boldsymbol{\Sigma}, \tag{3}$$

where we define

$$\boldsymbol{\Delta} := \begin{bmatrix} m_{3/2} & -m_{3/2} & & & & & \\ -m_{3/2} & m_{3/2}+m_{5/2} & -m_{5/2} & & & & \\ & \ddots & \ddots & \ddots & & & \\ & & & -m_{n-3/2} & m_{n-3/2}+m_{n-1/2} & -m_{n-1/2} \\ & & & & -m_{n-1/2} & m_{n-1/2} \end{bmatrix},$$

$$\boldsymbol{\Sigma} := \begin{bmatrix} m_{\mathrm{h},1} & & & -m_{\mathrm{h},1} & & & \\ & \ddots & & \vdots & & & \\ & & m_{\mathrm{h},j_0-1} & -m_{\mathrm{h},j_0-1} & & & \\ -m_{\mathrm{h},1} & \cdots & -m_{\mathrm{h},j_0-1} & \sum_{\substack{j=1 \\ j\neq j_0}}^{n} m_{\mathrm{h},j} & -m_{\mathrm{h},j_0+1} & \cdots & -m_{\mathrm{h},n} \\ & & & -m_{\mathrm{h},j_0+1} & m_{\mathrm{h},j_0+1} & & \\ & & & \vdots & & \ddots & \\ & & & -m_{\mathrm{h},n} & & & m_{\mathrm{h},n} \end{bmatrix}. \tag{4}$$

With this notation, we rewrite (1) for the vectors $\boldsymbol{S}, \boldsymbol{E}, \boldsymbol{I}, \boldsymbol{R} \in \mathbb{R}^n$ as

$$\begin{aligned} \frac{\mathrm{d}\boldsymbol{S}}{\mathrm{d}t} &= -\boldsymbol{\varphi}(\boldsymbol{S},\boldsymbol{E},\boldsymbol{I},\boldsymbol{R}) + \boldsymbol{M}\boldsymbol{S}, & \frac{\mathrm{d}\boldsymbol{I}}{\mathrm{d}t} &= \kappa\boldsymbol{E} - \gamma\boldsymbol{I} + \boldsymbol{M}\boldsymbol{I}, \\ \frac{\mathrm{d}\boldsymbol{E}}{\mathrm{d}t} &= \boldsymbol{\varphi}(\boldsymbol{S},\boldsymbol{E},\boldsymbol{I},\boldsymbol{R}) - \kappa\boldsymbol{E} + \boldsymbol{M}\boldsymbol{E}, & \frac{\mathrm{d}\boldsymbol{R}}{\mathrm{d}t} &= \gamma\boldsymbol{I} + \boldsymbol{M}\boldsymbol{R}, \end{aligned} \tag{5}$$

where the j-th component φ_j of $\boldsymbol{\varphi} = (\varphi_1, \ldots, \varphi_n)^{\mathrm{T}}$ is given by

$$\varphi_j(\boldsymbol{S},\boldsymbol{E},\boldsymbol{I},\boldsymbol{R}) = \beta_j \varphi(S_j, E_j, I_j, R_j),$$

where we define the scalar function

$$\varphi(S_j, E_j, I_j, R_j) := \frac{S_j I_j}{S_j + E_j + I_j + R_j} = \frac{S_j I_j}{N_j}.$$

2.2. **Some comments on the SEIR transmission model.** To put the formulation of the SEIR transmission model into the proper perspective, we first mention that an overview on discrete spatial heterogeneity concepts for compartmental epidemic models is provided by van den Driessche [19]. This includes, in particular, the approach by Sattenspiel and Dietz [40], which was the first epidemic patch model to involve geographic mobility, and which was later extended in [6]. These models include quite involved descriptions of the mobility and transmission processes since for each compartment of the underlying epidemic model (e.g., SIR or SEIR model), both the region of origin and the region of visit at time t are kept track of, which gives rise to $3n^2$ or $4n^2$ ordinary differential equations. For our purpose it is sufficient to keep track of the compartments in each region at each moment irrespective of origins of the individuals involved, for which a model of the type (1) is sufficient. In fact, most analyses of multigroup epidemic models refer to that situation (cf., e.g., [1, 20, 30–32, 47]). Further simplifications inherent in (1) (in comparison with the cited papers) arise from the assumption that the time scale of the pandemic is short enough so that natural birth and death rates can be neglected but long enough to warrant symmetric mobility rates as expressed by the rules governing mobility, and which cause the matrix $\boldsymbol{M}$ to be symmetric. The latter assumption of dominantly short-period travels is also supported by the observation that the pandemic took part in the southern winter of 2009, well after the summer school

holiday period during which substantial part of the metropolitan population would undertake trips of several weeks to other regions.

In light of all these assumptions it is straightforward to verify that the mobility model satisfies a conservation law of mixing in the following sense. Since $\boldsymbol{M}$ is symmetric and satisfies

$$-m_{ii} = \sum_{\substack{j=1 \\ j\neq i}} m_{ij} \quad \text{for all } i = 1, \ldots, n, \tag{6}$$

we obtain for each compartment $X \in \{S, E, I, R\}$ and the pure mobility process (i.e., we set the epidemiological rate parameters $\boldsymbol{\beta}$, κ and γ to zero) the identity

$$\begin{aligned} \frac{\mathrm{d}}{\mathrm{d}t} \sum_{i=1}^{n} X_i = \sum_{i=1}^{n} \mathcal{M}_i(X) = \sum_{i,j=1}^{n} m_{ij} X_j = \sum_{i=1}^{n} \left(\sum_{j=1, j\neq i}^{n} m_{ij} X_j + m_{ii} X_i \right) \\ = \sum_{i=1}^{n} \sum_{j=1, j\neq i}^{n} m_{ij} (X_j - X_i) = \sum_{i,j=1}^{n} m_{ij} X_j - \sum_{i,j=1}^{n} m_{ij} X_i = 0. \end{aligned} \tag{7}$$

A thorough analysis of the properties of the movement matrix $\boldsymbol{M}$ in a more general context is provided by Arino [4].

Furthermore, we assume that the mobility (travel) behaviour of all groups (epidemiological compartments) is the same; in particular infectious people travel to various regions during the pandemic. This assumption is also made explicitly in various alternative treatments and is usually justified by the (assumed) mild nature of the disease (cf., e.g., [19, p. 184], [40, p. 76], [4, p. 70] and [31, p. 1378]). Specifically for our case, [45] is a comprehensive reference because it presents a multi-country analysis of influenza mortality data during the 2009 A/H1N1 influenza pandemic.

2.3. **Stability of disease-free equilibrium (DFE) points.** We now look for disease-free equilibrium (DFE) points, i.e., equilibrium points with $\boldsymbol{E} = \boldsymbol{I} = \boldsymbol{R} = \boldsymbol{0}$. The equilibrium condition is obtained by setting the right-hand sides of equations (5) to zero and for $\boldsymbol{E} = \boldsymbol{I} = \boldsymbol{R} = \boldsymbol{0}$ it is equivalent to $\boldsymbol{M}\boldsymbol{S} = \boldsymbol{0}$, that is, $\boldsymbol{S} \in \mathcal{N}(\boldsymbol{M})$, where $\mathcal{N}$ denotes the nullspace of its matrix argument. The following proposition deals with this situation.

Proposition 2.1. *The matrices $\boldsymbol{\Delta}$ and $\boldsymbol{\Sigma}$ are positive semidefinite with a common nullspace $\mathcal{N}(\boldsymbol{\Delta}) = \mathcal{N}(\boldsymbol{\Sigma})$ spanned by $\boldsymbol{e} := (1, \ldots, 1)^{\mathrm{T}}$. For any choice of*

$$m_{i+1/2} > 0 \quad \text{for } i = 1, \ldots, n-1; \quad m_{\mathrm{h},i} > 0 \quad \text{for } i = 1, \ldots, n,\ i \neq j_0, \tag{8}$$

the matrix $\boldsymbol{M}$ is negative semidefinite and $\mathcal{N}(\boldsymbol{M}) = \langle \boldsymbol{e} \rangle$.

Proof. For a vector $\boldsymbol{y} = (y_1, \ldots, y_n)^{\mathrm{T}} \in \mathbb{R}^n$ we have

$$\begin{aligned} \boldsymbol{y}^{\mathrm{T}} \boldsymbol{\Delta} \boldsymbol{y} &= m_{3/2} y_1^2 + \sum_{i=2}^{n-1} (m_{i-1/2} + m_{i+1/2}) y_i^2 + m_{n-1/2} y_n^2 - 2 \sum_{i=1}^{n-1} m_{i+1/2} y_i y_{i+1} \\ &= \sum_{i=1}^{n-1} m_{i+1/2} (y_i - y_{i+1})^2 \geq 0. \end{aligned}$$

Since $\boldsymbol{\Delta}$ is symmetric, this identity implies that

$$\boldsymbol{y} \in \mathcal{N}(\boldsymbol{\Delta}) \Leftrightarrow \boldsymbol{y}^{\mathrm{T}} \boldsymbol{\Delta} \boldsymbol{y} = 0 \Leftrightarrow y_i = y_{i+1} \text{ for } i = 1, \ldots, n-1 \Leftrightarrow \boldsymbol{y} = \alpha \boldsymbol{e}$$

for some $\alpha \in \mathbb{R}$. Similarly we calculate

$$\boldsymbol{y}^{\mathrm{T}}\boldsymbol{\Sigma}\boldsymbol{y} = \sum_{\substack{i=1\\ i\neq j_0}}^{n} m_{\mathrm{h},i}\big(y_i^2 + y_{j_0}^2\big) - 2\sum_{\substack{i=1\\ i\neq j_0}}^{n} m_{\mathrm{h},i} y_i y_{j_0} = \sum_{\substack{i=1\\ i\neq j_0}}^{n} m_{\mathrm{h},i}(y_i - y_{j_0})^2 \geq 0,$$

and $\boldsymbol{y} \in \mathcal{N}(\boldsymbol{\Sigma}) \Leftrightarrow \boldsymbol{y}^{\mathrm{T}}\boldsymbol{\Sigma}\boldsymbol{y} = 0 \Leftrightarrow y_i = y_{j_0}$ for $i = 1, \ldots, n \Leftrightarrow \boldsymbol{y} = \tilde{\alpha}\boldsymbol{e}$ for some $\tilde{\alpha} \in \mathbb{R}$. In light of (8) and

$$\boldsymbol{y}^{\mathrm{T}}\boldsymbol{M}\boldsymbol{y} = -\boldsymbol{y}^{\mathrm{T}}\boldsymbol{\Delta}\boldsymbol{y} - \boldsymbol{y}^{\mathrm{T}}\boldsymbol{\Sigma}\boldsymbol{y}, \tag{9}$$

it now follows that $\boldsymbol{y}^{\mathrm{T}}\boldsymbol{M} \leq 0$. As mentioned above, $\boldsymbol{M} = \boldsymbol{M}^{\mathrm{T}}$ implies $\mathcal{N}(\boldsymbol{M}) = \{\boldsymbol{y} : \boldsymbol{y}^{\mathrm{T}}\boldsymbol{M}\boldsymbol{y} = 0\}$, and (9) therefore yields that $\mathcal{N}(\boldsymbol{M}) = \mathcal{N}(\boldsymbol{\Delta}) \cap \mathcal{N}(\boldsymbol{\Sigma}) = \langle \boldsymbol{e} \rangle$. □

Corollary 2.1. *The disease-free equilibrium (DFE) point for the metapopulation model with local and non-local migration* (5) *is given by*

$$S_j = N_{\mathrm{Total}}/n; \quad E_j = I_j = R_j = 0 \quad \text{for } j = 1, \ldots, n.$$

Proof. The DFE points are characterized by $\boldsymbol{E} = \boldsymbol{I} = \boldsymbol{R} = \boldsymbol{0}$ and, as seen above, $\boldsymbol{S} \in \mathcal{N}(\boldsymbol{M})$, which is spanned by $\boldsymbol{e}$, i.e., $S_j = S_*$, for $j = 1, \ldots, n$. Since

$$N_{\mathrm{Total}} = \sum_{j=1}^{n}(S_j(t) + E_j(t) + I_j(t) + R_j(t)) \quad \text{for all } t,$$

it follows that $N_{\mathrm{Total}} = nS_*$, that is, $S_j = S_* = N_{\mathrm{Total}}/n$. □

The basic reproduction number ($\mathcal{R}_0$) quantifies the expected number of secondary cases generated by a primary infectious individual during the infectious period in a completely susceptible population [16]. In our model with different transmission rates across regions, the local reproduction number $\mathcal{R}_{0,j}$ for region j is given by $\mathcal{R}_{0,j} = \beta_j/\gamma$. We are interested in the analysis of the stability of the DFE for system (5), which captures the overall transmissibility for the entire metapopulation.

To analyze the stability of these equilibria we linearize (5) about $(\bar{\boldsymbol{S}}, \bar{\boldsymbol{E}}, \bar{\boldsymbol{I}}, \bar{\boldsymbol{R}}) \in \mathbb{R}^{4n}$. Assuming that $(\hat{\boldsymbol{S}}, \hat{\boldsymbol{E}}, \hat{\boldsymbol{I}}, \hat{\boldsymbol{R}})$ is a small displacement from equilibrium, we get the first-order approximations (in the displacement)

$$\begin{aligned}
&\varphi_j(\bar{\boldsymbol{S}} + \hat{\boldsymbol{S}}, \bar{\boldsymbol{E}} + \hat{\boldsymbol{E}}, \bar{\boldsymbol{I}} + \hat{\boldsymbol{I}}, \bar{\boldsymbol{R}} + \hat{\boldsymbol{R}}) \\
&\approx \left(\frac{\bar{I}_j}{\bar{N}_j} - \frac{\bar{I}_j\bar{S}_j}{\bar{N}^2}\right)\hat{S}_j + \left(\frac{\bar{S}_j}{\bar{N}_j} - \frac{\bar{I}_j\bar{S}_j}{\bar{N}_j^2}\right)\hat{I}_j - \frac{\bar{I}_j\bar{S}_j}{\bar{N}_j^2}\hat{E}_j - \frac{\bar{I}_j\bar{S}_j}{\bar{N}_j^2}\hat{R}_j, \\
&\varphi_j(\bar{\boldsymbol{S}} + \hat{\boldsymbol{S}}, \boldsymbol{0} + \hat{\boldsymbol{E}}, \boldsymbol{0} + \hat{\boldsymbol{I}}, \boldsymbol{0} + \hat{\boldsymbol{R}}) \approx \frac{\bar{S}_j}{\bar{N}_j}\hat{I}_j = \hat{I}_j.
\end{aligned}$$

The linearized version of (5) can be written in matrix-vector form as

$$\frac{\mathrm{d}}{\mathrm{d}t}\begin{pmatrix}\hat{\boldsymbol{S}}\\ \hat{\boldsymbol{E}}\\ \hat{\boldsymbol{I}}\\ \hat{\boldsymbol{R}}\end{pmatrix} = \boldsymbol{Z}\begin{pmatrix}\hat{\boldsymbol{S}}\\ \hat{\boldsymbol{E}}\\ \hat{\boldsymbol{I}}\\ \hat{\boldsymbol{R}}\end{pmatrix}, \quad \boldsymbol{Z} = \begin{bmatrix}\boldsymbol{M} & \boldsymbol{0} & -\boldsymbol{G} & \boldsymbol{0}\\ \boldsymbol{0} & \boldsymbol{M}-\boldsymbol{C} & \boldsymbol{G} & \boldsymbol{0}\\ \boldsymbol{0} & \boldsymbol{C} & \boldsymbol{M}-\boldsymbol{D} & \boldsymbol{0}\\ \boldsymbol{0} & \boldsymbol{0} & \boldsymbol{D} & \boldsymbol{M}\end{bmatrix},$$

with the following notation, where $\boldsymbol{\mathcal{I}}_n$ is the $n \times n$ identity matrix:

$$\boldsymbol{G} := \mathrm{diag}(\beta_1, \ldots, \beta_n), \quad \boldsymbol{C} := \kappa\boldsymbol{\mathcal{I}}_n, \quad \boldsymbol{D} := \gamma\boldsymbol{\mathcal{I}}_n.$$

The stability of the DFE amounts to asserting whether $\mathrm{Re}(\lambda(\boldsymbol{Z})) \le 0$ for any eigenvalue $\lambda(\boldsymbol{Z})$ of $\boldsymbol{Z}$. Since the eigenvalues of $\boldsymbol{M}$ are nonpositive and

$$\det(\boldsymbol{Z} - \lambda \boldsymbol{\mathcal{I}}_{4n}) = \det(\boldsymbol{M} - \lambda \boldsymbol{\mathcal{I}}_n)^2 \det(\boldsymbol{Z}_1 - \lambda \boldsymbol{\mathcal{I}}_{2n}), \quad \boldsymbol{Z}_1 := \begin{bmatrix} \boldsymbol{M} - \boldsymbol{C} & \boldsymbol{G} \\ \boldsymbol{C} & \boldsymbol{M} - \boldsymbol{D} \end{bmatrix},$$

it follows that $\mathrm{Re}(\lambda(\boldsymbol{Z})) \le 0$ is equivalent to $\mathrm{Re}(\lambda(\boldsymbol{Z}_1)) \le 0$. Note that $\boldsymbol{Z}_1$ is the coefficient matrix of the $(\hat{\boldsymbol{E}}, \hat{\boldsymbol{I}})$ subsystem, i.e.,

$$\frac{\mathrm{d}}{\mathrm{d}t} \begin{pmatrix} \hat{\boldsymbol{E}} \\ \hat{\boldsymbol{I}} \end{pmatrix} = \boldsymbol{Z}_1 \begin{pmatrix} \hat{\boldsymbol{E}} \\ \hat{\boldsymbol{I}} \end{pmatrix}.$$

Proposition 2.2. *For any (compatible) matrices $\boldsymbol{\mathcal{A}}$, $\boldsymbol{\mathcal{B}}$, $\boldsymbol{\mathcal{C}}$ and $\boldsymbol{\mathcal{D}}$ we have*

$$\det \begin{bmatrix} \boldsymbol{\mathcal{A}} & \boldsymbol{\mathcal{B}} \\ \boldsymbol{\mathcal{C}} & \boldsymbol{\mathcal{D}} \end{bmatrix} = \det \boldsymbol{\mathcal{A}} \det(\boldsymbol{\mathcal{D}} - \boldsymbol{\mathcal{C}}\boldsymbol{\mathcal{A}}^{-1}\boldsymbol{\mathcal{B}}). \tag{10}$$

Furthermore, if all matrices have the same dimension and $\boldsymbol{\mathcal{C}}$ and $\boldsymbol{\mathcal{A}}$ commute, then

$$\det \begin{bmatrix} \boldsymbol{\mathcal{A}} & \boldsymbol{\mathcal{B}} \\ \boldsymbol{\mathcal{C}} & \boldsymbol{\mathcal{D}} \end{bmatrix} = \det(\boldsymbol{\mathcal{A}}\boldsymbol{\mathcal{D}} - \boldsymbol{\mathcal{C}}\boldsymbol{\mathcal{B}}). \tag{11}$$

Proof. Assertion (10) follows from elementary properties of the determinant function and the identity

$$\begin{bmatrix} \boldsymbol{\mathcal{A}} & \boldsymbol{\mathcal{B}} \\ \boldsymbol{\mathcal{C}} & \boldsymbol{\mathcal{D}} \end{bmatrix} = \begin{bmatrix} \boldsymbol{\mathcal{I}} & \boldsymbol{0} \\ \boldsymbol{\mathcal{C}}\boldsymbol{\mathcal{A}}^{-1} & \boldsymbol{\mathcal{I}} \end{bmatrix} \begin{bmatrix} \boldsymbol{\mathcal{A}} & \boldsymbol{\mathcal{B}} \\ \boldsymbol{0} & \boldsymbol{\mathcal{D}} - \boldsymbol{\mathcal{C}}\boldsymbol{\mathcal{A}}^{-1}\boldsymbol{\mathcal{B}} \end{bmatrix}.$$

If $\boldsymbol{\mathcal{C}}$ and $\boldsymbol{\mathcal{A}}$ commute, then (11) follows from

$$\begin{aligned} \det \boldsymbol{\mathcal{A}} \det(\boldsymbol{\mathcal{D}} - \boldsymbol{\mathcal{C}}\boldsymbol{\mathcal{A}}^{-1}\boldsymbol{\mathcal{B}}) &= \det\big(\boldsymbol{\mathcal{A}}(\boldsymbol{\mathcal{D}} - \boldsymbol{\mathcal{C}}\boldsymbol{\mathcal{A}}^{-1}\boldsymbol{\mathcal{B}})\big) = \det(\boldsymbol{\mathcal{A}}\boldsymbol{\mathcal{D}} - \boldsymbol{\mathcal{A}}\boldsymbol{\mathcal{C}}\boldsymbol{\mathcal{A}}^{-1}\boldsymbol{\mathcal{B}}) \\ &= \det(\boldsymbol{\mathcal{A}}\boldsymbol{\mathcal{D}} - \boldsymbol{\mathcal{C}}\boldsymbol{\mathcal{B}}). \end{aligned}$$

□

In light of the previous discussion, we see that the DFE is stable if all zeros $\lambda(\boldsymbol{Z}_1)$ of $\det(\boldsymbol{Z}_1 - \lambda \boldsymbol{I}_{2n})$ satisfy $\mathrm{Re}(\lambda(\boldsymbol{Z}_1)) \le 0$. Satisfaction of this condition is difficult to analyze for a general mobility matrix (3), (4) and transmission parameters $\boldsymbol{\beta}$, even using a next-generation matrix analysis (see [17,21]), but two simple sub-cases (namely either $\boldsymbol{\beta} = \beta \boldsymbol{e}$ or $\boldsymbol{M} = \boldsymbol{0}$, which are certainly unrealistic) can be handled easily (Lemmas 2.1 and 2.2). For general values of these parameters we can only provide a sufficient criterion of stability of the DFE (Lemma 2.3) in terms of the basic reproduction number in each region being below 1.

The following result was already obtained in [5]. We include it here for the sake of completeness.

Lemma 2.1. *Assume that $\boldsymbol{\beta} = \beta \boldsymbol{e}$. Then the all-susceptible equilibria are stable if and only if*

$$\mathcal{R}_0 = \beta/\gamma < 1. \tag{12}$$

Proof. With $\beta_i = \beta$, $\boldsymbol{G} = \beta \boldsymbol{\mathcal{I}}_n$ and applying Proposition 2.2 to $\det(\boldsymbol{Z}_1 - \lambda \boldsymbol{\mathcal{I}}_{2n})$, we deduce that

$$\det(\boldsymbol{Z}_1 - \lambda \boldsymbol{\mathcal{I}}_{2n}) = \det\big(\big[\boldsymbol{M} - (\kappa + \lambda)\boldsymbol{\mathcal{I}}_n\big]\big[\boldsymbol{M} - (\gamma + \lambda)\boldsymbol{\mathcal{I}}_n\big] - \kappa\beta \boldsymbol{\mathcal{I}}_n\big).$$

Since $\boldsymbol{M}$ is symmetric and negative semidefinite, we have $\boldsymbol{M} = \boldsymbol{P}\tilde{\boldsymbol{M}}\boldsymbol{P}^{\mathrm{T}}$ for an orthogonal matrix $\boldsymbol{P}$ and $\tilde{\boldsymbol{M}} = \operatorname{diag}(\mu_1, \ldots, \mu_n)$, where $\mu_i \leq 0$. At least one μ_i equals zero (say, $\mu_1 = 0$) since $\boldsymbol{M}$ is singular. Since

$$\begin{aligned}&\boldsymbol{P}^{\mathrm{T}}\big(\big[\boldsymbol{M} - (\kappa+\lambda)\boldsymbol{\mathcal{I}}_n\big]\big[\boldsymbol{M} - (\gamma+\lambda)\boldsymbol{\mathcal{I}}_n\big] - \kappa\beta\boldsymbol{\mathcal{I}}_n\big)\boldsymbol{P}\\ &= \big[\tilde{\boldsymbol{M}} - (\kappa+\lambda)\boldsymbol{\mathcal{I}}_n\big]\big[\tilde{\boldsymbol{M}} - (\gamma+\lambda)\boldsymbol{\mathcal{I}}_n\big] - \kappa\beta\boldsymbol{\mathcal{I}}_n\end{aligned}$$

is diagonal and $\det \boldsymbol{P} = \det \boldsymbol{P}^{\mathrm{T}} = \pm 1$, we get

$$\begin{aligned}&\det\big(\big[\boldsymbol{M} - (\kappa+\lambda)\boldsymbol{\mathcal{I}}_n\big]\big[\boldsymbol{M} - (\gamma+\lambda)\boldsymbol{\mathcal{I}}_n\big] - \kappa\beta\boldsymbol{\mathcal{I}}_n\big)\\ &= \det\big(\boldsymbol{P}^{\mathrm{T}}\big\{\big[\boldsymbol{M} - (\kappa+\lambda)\boldsymbol{\mathcal{I}}_n\big]\big[\boldsymbol{M} - (\gamma+\lambda)\boldsymbol{\mathcal{I}}_n\big] - \kappa\beta\boldsymbol{\mathcal{I}}_n\big\}\boldsymbol{P}\big)\\ &= \det\big(\big[\tilde{\boldsymbol{M}} - (\kappa+\lambda)\boldsymbol{\mathcal{I}}_n\big]\big[\tilde{\boldsymbol{M}} - (\gamma+\lambda)\boldsymbol{\mathcal{I}}_n\big] - \kappa\beta\boldsymbol{\mathcal{I}}_n\big)\\ &= \prod_{i=1}^{n}\big((\mu_i - \kappa - \lambda)(\mu_i - \gamma - \lambda) - \kappa\beta\big).\end{aligned}$$

Thus, the eigenvalues $\lambda_i^{\pm}$, $i = 1, \ldots, n$ of $\boldsymbol{Z}_1$ are the roots of the quadratic equations

$$(\mu_i - \kappa - \lambda)(\mu_i - \gamma - \lambda) - \kappa\beta = 0, \quad i = 1, \ldots, n,$$

namely

$$\lambda_i^{\pm} = \frac{1}{2}\Big(2\mu_i - \gamma - \kappa \pm \sqrt{(2\mu_i - \gamma - \kappa)^2 - 4\big((\mu_i - \gamma)(\mu_i - \kappa) - \kappa\beta\big)}\Big)$$

for $i = 1, \ldots, n$. Since $\mu_i \leq 0$ and $\gamma, \kappa > 0$, we have $\operatorname{Re}\lambda_i^{\pm} < 0$ if and only if

$$(\mu_i - \gamma)(\mu_i - \kappa) > \kappa\beta. \tag{13}$$

In view of $(\mu_i - \gamma)(\mu_i - \kappa) - \kappa\gamma = \mu_i(\mu_i - \kappa - \gamma) > 0$, a sufficient condition for (13) to hold is $\gamma > \beta$, i.e., (12). This condition is also necessary, as can be deduced from evaluating (13) for $\mu_i = \mu_1 = 0$. □

Lemma 2.2. *Assume that $m_{i+1/2} = 0$ and $m_{\mathrm{h},i} = 0$ for all i. Then the all-susceptible equilibria are stable if and only if $\mathcal{R}_{0,i} = \beta_i/\gamma < 1$ for $i = 1, \ldots, n$.*

Proof. Proposition 2.2 applied to $\det(\boldsymbol{Z}_1 - \lambda\boldsymbol{\mathcal{I}}_{2n})$ yields

$$\begin{aligned}\det(\boldsymbol{Z}_1 - \lambda\boldsymbol{\mathcal{I}}_{2n}) &= \det\big(\big[-(\kappa+\lambda)\boldsymbol{\mathcal{I}}_n\big]\big[-(\gamma+\lambda)\boldsymbol{\mathcal{I}}_n\big] - \kappa\boldsymbol{G}\big)\\ &= \det\big(\operatorname{diag}\big((\gamma+\lambda)(\kappa+\lambda) - \kappa\beta_i\big)\big)\\ &= \prod_{i=1}^{n}(\lambda^2 + (\kappa+\gamma)\lambda + \kappa(\gamma - \beta_i)).\end{aligned}$$

The roots of this polynomial are

$$\lambda_i^{\pm} = \frac{1}{2}\Big(-\gamma - \kappa \pm \sqrt{(\gamma+\kappa)^2 - 4\kappa(\gamma - \beta_i)}\Big)$$

for $i = 1, \ldots, n$. Since $\gamma, \kappa > 0$, we have $\operatorname{Re}\lambda_i^{\pm} < 0$ if and only if $\gamma > \beta_i$. □

It remains to analyze the remaining cases, for which β_i are different and $\boldsymbol{M} \neq \boldsymbol{0}$. As in the previous cases, we perform a simple and direct analysis of the eigenvalues of the matrix $\boldsymbol{Z}_1$ governing the dynamics of the exposed-infectious population.

Lemma 2.3. *A sufficient condition for the DFE to be stable is*

$$\mathcal{R}_{0,i} = \beta_i/\gamma < 1 \quad \text{for } i = 1, \ldots, n. \tag{14}$$

Proof. We apply the Gershgorin circle theorem columnwise to $\boldsymbol{Z}_1$. Since the matrix $\boldsymbol{M}$ has negative diagonal entries, nonnegative off-diagonal entries and satisfies (6), the circles corresponding to the first n columns of $\boldsymbol{Z}_1$ have center $m_{jj}-\kappa$ and radius $\sum_{i\neq j} m_{ij} + \kappa = -(m_{jj}-\kappa)$, and therefore are included in $\mathbb{C}_- = \{z \in \mathbb{C} : \operatorname{Re} z \leq 0\}$ and its intersection with $\mathbb{C}_0 = \{z \in \mathbb{C} : \operatorname{Re} z = 0\}$ is $\{0\}$. Likewise, the circles corresponding to the last n columns of $\boldsymbol{Z}_1$ have center $c_j = m_{jj} - \gamma$ and radius

$$\sum_{i\neq j} m_{ij} + \beta_j < -m_{jj} + \gamma = -c_j, \tag{15}$$

and are therefore also included in $\mathbb{C}_-$ and their intersection with $\mathbb{C}_0$ is empty.

We conclude that all Gershgorin circles of $\boldsymbol{Z}_1$ are included in $\mathbb{C}_-$ and therefore all eigenvalues of $\boldsymbol{Z}_1$ have nonpositive real parts. Furthermore, using that the matrices $\boldsymbol{M} - \kappa\boldsymbol{\mathcal{I}}_n$ and $\boldsymbol{M} - \gamma\boldsymbol{\mathcal{I}}_n$ are irreducible we conclude that $\boldsymbol{Z}_1$ is irreducible. Since the strict inequality holds in (15), we know that $\boldsymbol{Z}_1^{\mathrm{T}}$ is an irreducibly diagonally dominant matrix, and therefore $\boldsymbol{Z}_1^{\mathrm{T}}$ and $\boldsymbol{Z}_1$ are regular. Thus, 0 is not an eigenvalue of $\boldsymbol{Z}_1$, and we conclude that all its eigenvalues have strictly negative real part. □

The other implication, namely that violation of (14), i.e., $\mathcal{R}_{0,i} \geq 1$ for *some* i, would imply that the DFE is *unstable*, is not true. This can be seen by a numerical counterexample. For $n = 3$ and $j_0 = 2$, consider $m_{\mathrm{h},i} = 0$ for $i = 1, 2, 3$, $m_{3/2} = m_{5/2} = 0.1$ and $\kappa = \gamma = 1$. We set $\beta_1 = \beta_2 = 0.5$ and $\beta_3 = 1.1$; note that $\beta_3/\gamma > 1$. Then we have

$$\boldsymbol{Z}_1 = \begin{bmatrix} -1.1 & 0.1 & 0 & 0.5 & 0 & 0 \\ 0.1 & -1.2 & 0.1 & 0 & 0.5 & 0 \\ 0 & 0.1 & -1.1 & 0 & 0 & 1.1 \\ 1 & 0 & 0 & -1.1 & 0.1 & 0 \\ 0 & 1 & 0 & 0.1 & -1.2 & 0.1 \\ 0 & 0 & 1 & 0 & 0.1 & -1.1 \end{bmatrix}.$$

For this matrix we obtain the eigenvalues

$$\{\lambda_1^{\pm}, \lambda_2^{\pm}, \lambda_3^{\pm}\} = \{-2.1892, -1.9358, -1.7376, -0.5697, -0.3400, -0.0277\},$$

so all eigenvalues of $\boldsymbol{Z}_1$ have negative real part, and therefore the DFE is stable, despite $\beta_3/\gamma > 1$.

This situation is the opposite to that found in [20] for other epidemiological models, in the sense that van den Driessche and coauthors prove that $\mathcal{R}_{0,i} \leq \mathcal{R}_0$, so that $\mathcal{R}_0 < 1$ implies $\mathcal{R}_{0,i} < 1$ for all i, but they show examples for which $\mathcal{R}_{0,i} < 1$ for all i, and yet $\mathcal{R}_0 > 1$.

3. **Epidemiological and population data.** We relied on a large individual-level dataset comprising all hospitalizations for severe acute respiratory infection (hereafter referred to as SARI) reported by all public and private hospitals to the Chilean Ministry of Health during 01-May to 31-December 2009 to characterize peak timing of the 2009 A/H1N1 influenza pandemic across 15 Chilean regions. A total of 1809 SARI hospitalizations (29.4%) were laboratory confirmed with A/H1N1 pandemic influenza. A previous study [12] reported a latitudinal gradient in peak pandemic timing, representing a 16–39-day lag in disease activity from the southern regions relative to the northernmost region ($P < 0.001$) as shown in Figure 1 (b). Maximum temperature and specific humidity together with other geographical differences in latitude of Chilean regions explained 68.5% of the variability in peak timing ($P = 0.01$). There was also a decreasing gradient in reproduction number

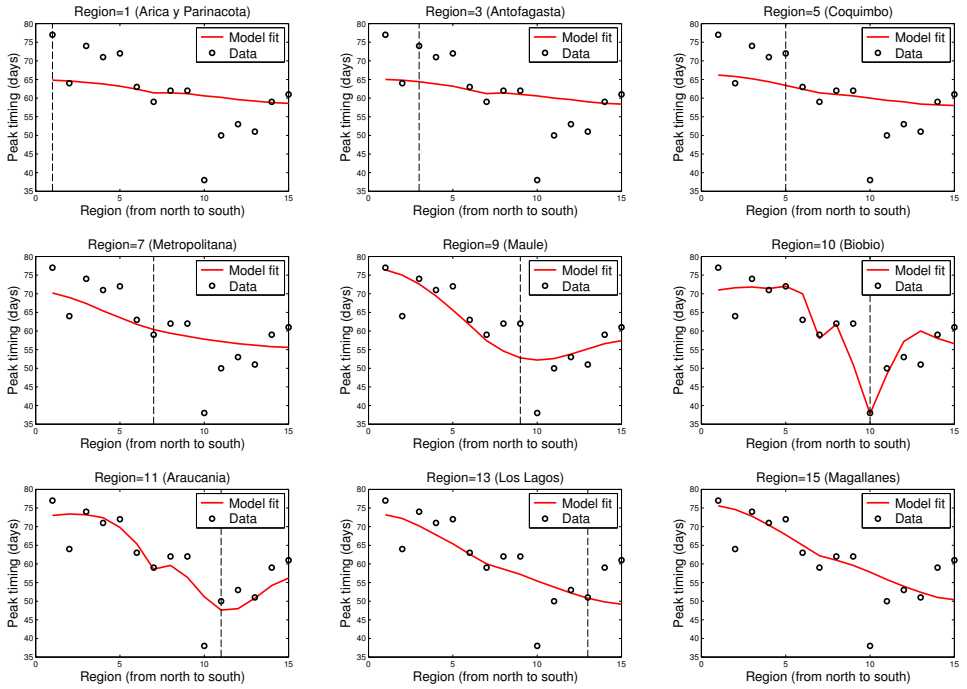

FIGURE 2. Model fits provided by our metapopulation model to the pandemic peak timing data of the 2009 A/H1N1 influenza pandemic across Chilean regions. The vertical dashed line marks the region where the initial number of infectious individuals is introduced.

from south to north Chile. The regional mean $\mathcal{R}_0$ estimates were 1.6–2.0, 1.3–1.5, and 1.2–1.3 for southern, central and northern regions, respectively [12].

To parametrize population size for each of the Chilean regions, we also obtained regional estimates of population size for 2009 from the Instituto Nacional de Estadísticas [25], see Table 1.

4. **Parameter estimates and initial conditions.** The latent period was set at $1/\kappa = 1.5\,\mathrm{d}$ and the infectious period was set at $1/\gamma = 1.5\,\mathrm{d}$ in line with influenza epidemiology [12]. The local basic reproduction number across Chilean regions varied according to a prior study [12]. Hence, the local transmission coefficient β_j for region j was chosen as

$$\beta_j = \gamma\left(1.2 + 0.4\frac{j-1}{n-1}\right), \quad j = 1, \ldots, n, \tag{16}$$

such that $\mathcal{R}_{0,j} = \beta_j/\gamma$ satisfies $\mathcal{R}_{0,1} = 1.2$ (northernmost region) and increases linearly across regions from north to south until $\mathcal{R}_{0,n} = 1.6$ (southernmost region). Moreover, we consider a simple scenario, denoted in what follows by "Scenario 1" in which the mobilities are given by two constants, namely

$$m_{j-1/2} = m \quad \text{for all } j = 2, \ldots, n, \quad m_{\mathrm{h},j} = m_{\mathrm{h}} \quad \text{for all } j = 1, \ldots, n. \tag{17}$$

(This will be contrasted later with the results obtained by an alternative Scenario 2 with variable mobilities.) We estimated the mobility parameters m and m_{h} and

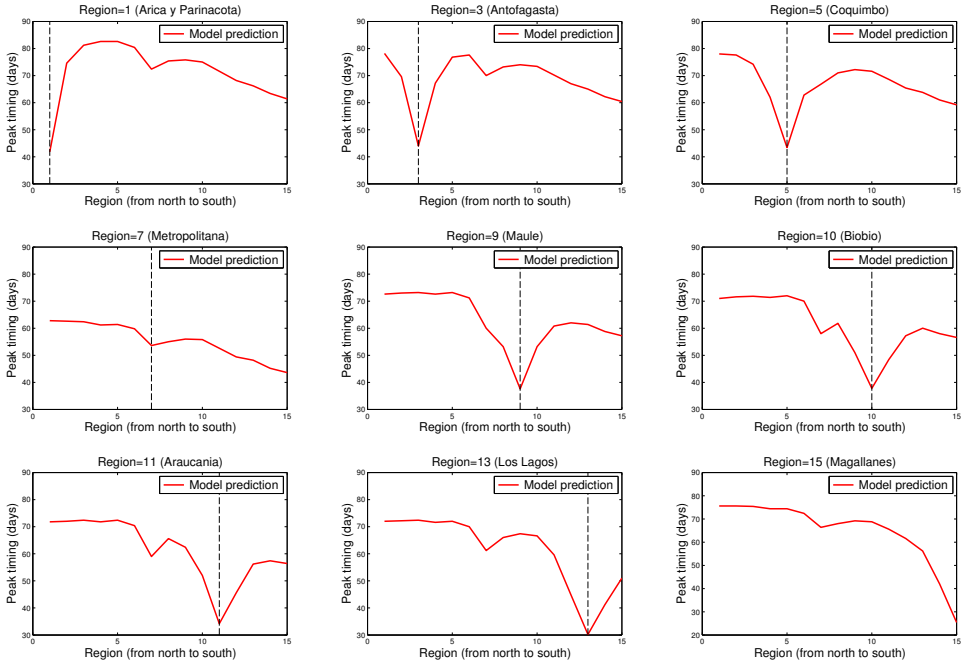

FIGURE 3. Predictions of pandemic peak timing based on our best fit parameter values (18) when the initial introduction of infectious cases varies from northern, central or southern regions.

the initial number of infectious individuals I_0 by least-squares fitting our metapopulation transmission model to data on pandemic peak timing of the 2009 A/H1N1 influenza pandemic across the 15 Chilean regions. This yields

$$m = 0.0046, \quad m_{\rm h} = 0.0065, \quad I_0 = 216. \tag{18}$$

Moreover, the entire regional populations were assumed to be susceptible at the beginning of the pandemic. We assessed model fits that assumed that the initial number of infectious individuals were located in northern, central or southern regions (see Figure 2), with the conclusion that placing a set of infectious individuals in region 10 (Biobío) yields the best fit to our pandemic peak timing data.

5. **Results and uncertainty and stability analysis.** Our model that considers an initial set of infectious individuals in region 10 (Biobío) yielded the best fit to our pandemic peak timing data of the 2009 A/H1N1 influenza pandemic across regions of Chile as shown in Figure 2. Our next best fit model was obtained when the initial number of infectious individuals were assumed to be located in the region 11 (Araucanía), south of region 10 (Biobío). Other model fits were of poorer quality particularly those with initial infectious introductions assumed in northern regions (Figure 2). The spatial-temporal progression of the pandemic simulated using our best-fit parameter values with an initial infectious focus in the Biobío region is shown in Figures 3 and 4. These results suggest that the pandemic peak timing follows a south-north gradient whenever the initial introduction of infectious cases occurs in central or southern regions. The global basic reproduction number was estimated at $\mathcal{R}_0 = 1.56$ based on the best-fit parameter estimates.

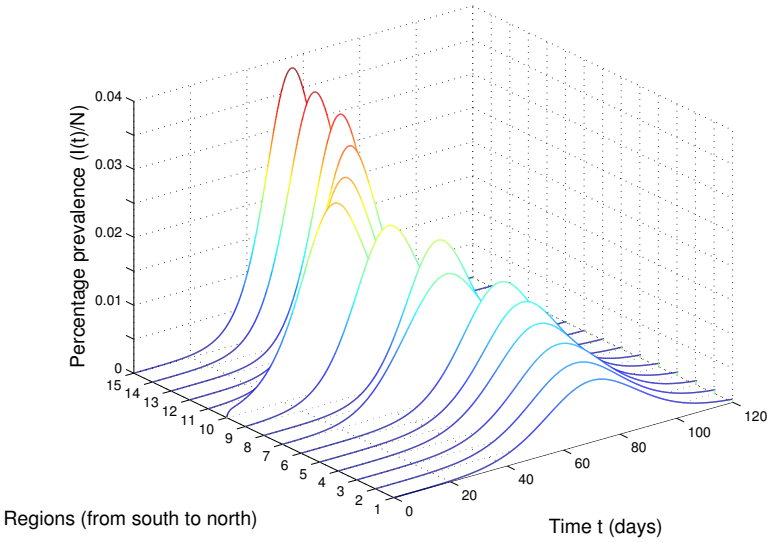

FIGURE 4. Spatial-temporal progression of pandemic influenza simulated across 15 Chilean regions based on our best model fit to peak timing data. The initial number of infectious individuals is set in the southern Biobío region. Parameters are given by (18).

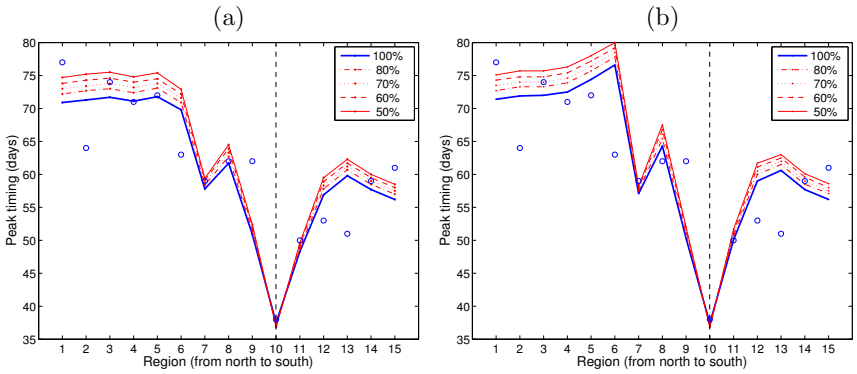

FIGURE 5. Predictions of pandemic peak timing when a varying fraction of infectious individuals are allowed to move to other regions according to the mobility parameters of (a) Scenario 1 (based on our best-fit parameter values), (b) Scenario 2. The vertical dashed line denotes region 10 (Biobío) where the initial number of infectious individuals is introduced.

We evaluated the sensitivity of our results with respect to variations of the transmission and mobility parameters. First of all, our results did not change significantly when only fraction of infectious individuals were allowed to move to other regions (Figure 5). Moreover, we computed the basic reproduction number $\mathcal{R}_0$ by the next-generation method [21] to evaluate the influence of the mobility parameters on the global values of $\mathcal{R}_0$. Here we limit ourselves to Scenario 1, (17), so that we can plot $\mathcal{R}_0$ as a function of m and m_{h}, see Figure 6. We found that the global $\mathcal{R}_0$

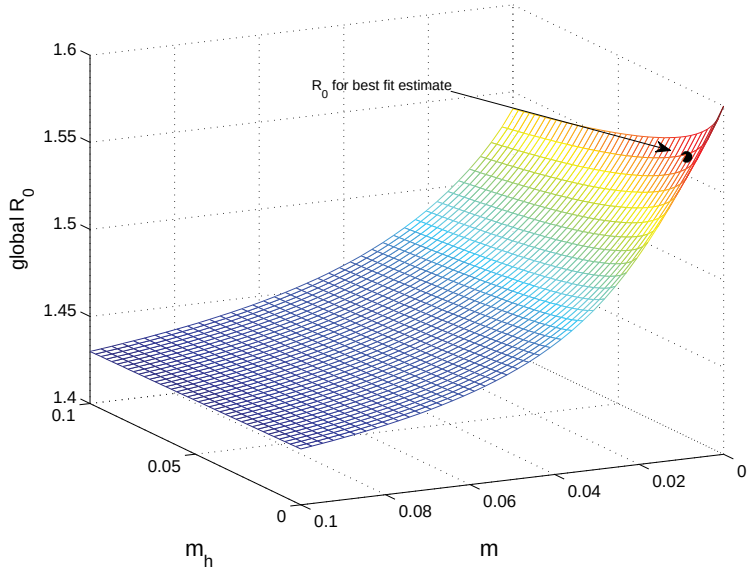

FIGURE 6. Basic reproduction number $\mathcal{R}_0$ as a function of parameters m and $m_{\rm h}$. Global $\mathcal{R}_0$ decreases as the mobility parameters m and $m_{\rm h}$ increase. The arrow points to the best fit estimates of m and $m_{\rm h}$ obtained by fitting our metapopulation transmission model to data on pandemic peak timing of the 2009 A/H1N1 influenza pandemic in Chile as explained in the text.

j	$m_{j-1/2}$	$m_{{\rm h},j}$	j	$m_{j-1/2}$	$m_{{\rm h},j}$	j	$m_{j-1/2}$	$m_{{\rm h},j}$
1	2.0	6.0	6	4.6	0	11	2.5	5.0
2	2.5	6.0	7	4.6	0	12	2.0	5.0
3	3.0	6.5	8	4.0	0	13	1.5	6.5
4	3.5	5.0	9	3.5	0	14	1.5	5.0
5	4.0	5	10	3.0	6.5	15	1.5	6.0

TABLE 2. Non-homogeneous mobility parameters, to be multiplied by 10^{-3}, chosen for Scenario 2.

declined as the mobility parameters m and $m_{\rm h}$ increased. For the special case when $m = m_{\rm h} = 0$, $\mathcal{R}_0$ is given by the maximum regional $\mathcal{R}_{0,j}$, which is given by 1.6 as originally set for the southernmost Chilean region. For both Scenario 1 and 2 we also assessed the influence of the values of the mobility parameters, i.e. m and $m_{\rm h}$ for Scenario 1 and $\boldsymbol{m}$ and $\boldsymbol{m}_h$ for Scenario 2, if these are reduced gradually. The results are shown in Figures 5 (a) and (b), respectively.

To study the effect of variations in the mobility parameters, we first define a second, and possibly more realistic mobility scenario by choosing the parameters $m_{j-1/2}$ and $m_{{\rm h},j}$ according to the values given in Table 2. These values roughly represent fluctuations in the territorial connectivity of Chile, in the sense that long distances between, say, the capitals of regions 1 and 2 (or 2 and 3) probably discourage habitants from these regions to undertake trips (so the values of $m_{j-1/2}$ are

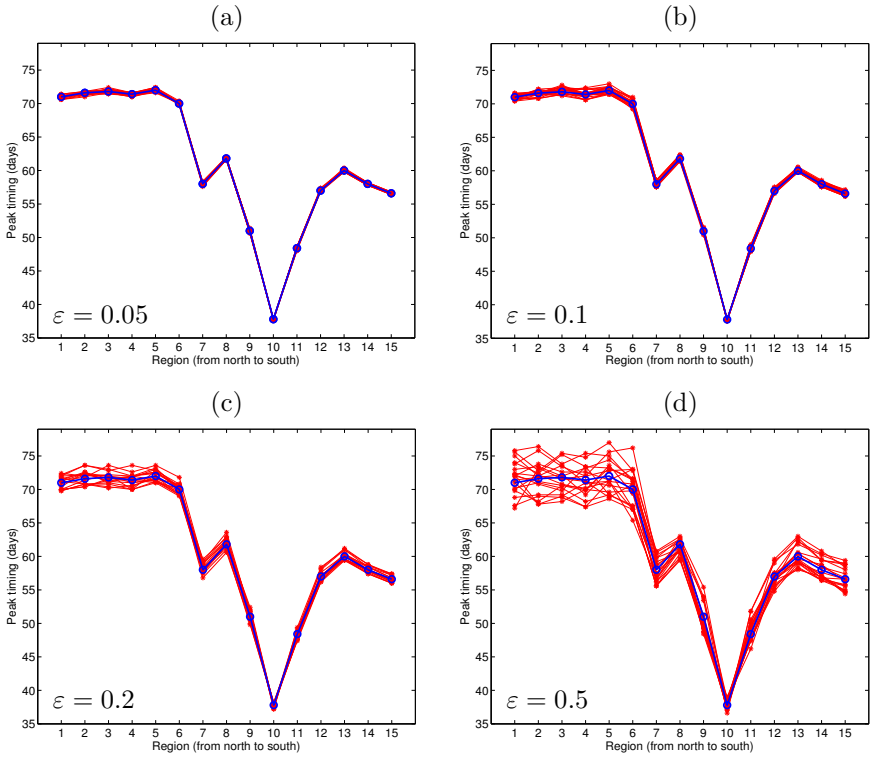

FIGURE 7. Scenario 1: (a–d) peak timing obtained by mobility parameters (17), (18) (blue curve), and 20 trajectories (red curves) of peak timing obtained by aleatoric variation (19), (20) of these parameters with the indicated values of ε. The transmission parameters $\boldsymbol{\beta}$ always have the values (16).

small), in contrast to the short distance e.g. between regions 6, 7 and 8 (large values of $m_{j-1/2}$). On the other hand, it is reasonable to assume that travel involving the hub region, and which is not included in the overland mobility rates $m_{j-1/2}$, corresponds to air travel, and is not done from regions relatively close to the hub region. For this reason we choose $m_{\mathrm{h},j} = 0$ in Scenario 2 for regions 6 to 9. The blue curve in Figure 7 (it is the same in all plots) shows the result of peak timing for Scenario 1, and the blue curve in all plots Figure 8 shows the corresponding result for Scenario 2. We observe that the results are very similar, which leads to the conjecture that the results are possibly only moderately sensitive to the choice of the mobility parameters. To test this hypothesis we proceed by Monte Carlo-type sampling as follows. We define the vectors

$$\boldsymbol{m} := (m_{3/2}, \ldots, m_{n-1/2}), \quad \boldsymbol{m}_{\mathrm{h}} := (m_{\mathrm{h},1}, \ldots, m_{\mathrm{h},n}), \quad \boldsymbol{m}^* := (\boldsymbol{m}, \boldsymbol{m}_{\mathrm{h}}). \tag{19}$$

Assume now that $(\theta_1, \ldots, \theta_{2n-1})$ is vector of random variables assuming values in $(-1, 1)$. We then perturb the parameter vector $\boldsymbol{m}^*$ by

$$\tilde{\boldsymbol{m}}^* = \big(\boldsymbol{\mathcal{I}}_{2n-1} + \varepsilon \operatorname{diag}(\theta_1, \ldots, \theta_{2n-1})\big)\boldsymbol{m}^*, \tag{20}$$

where $\varepsilon \geq 0$ is a parameter that controls the relative size of the perturbation (note that $\|\tilde{\boldsymbol{m}}^* - \boldsymbol{m}^*\|_\infty / \|\boldsymbol{m}^*\|_\infty \leq \varepsilon$). Each of the plots of Figure 7 includes 20

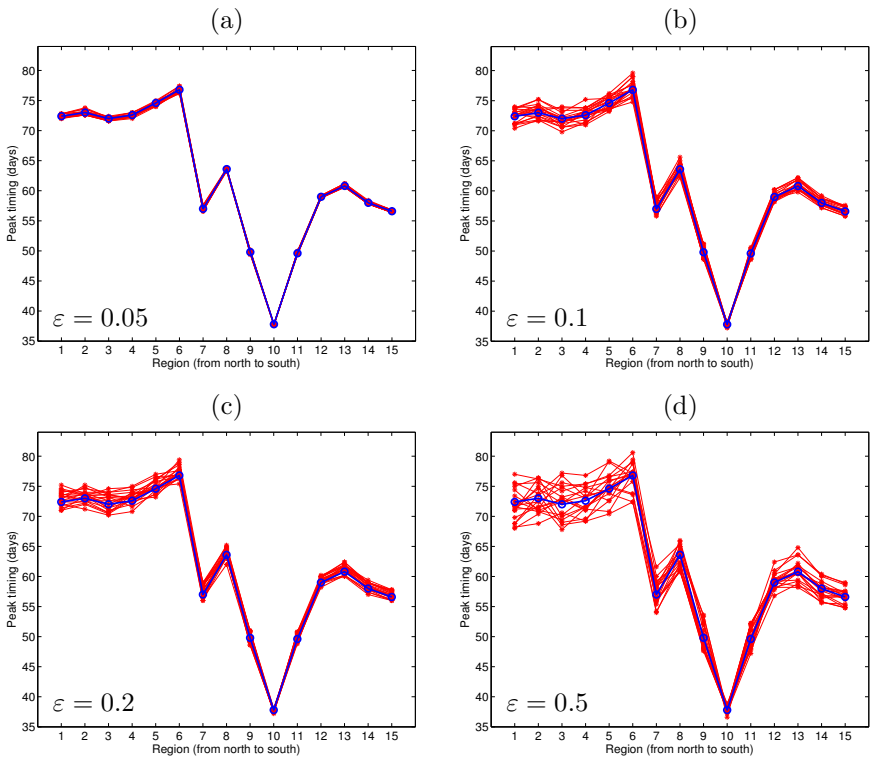

FIGURE 8. Scenario 2: (a–d) peak timing obtained by the mobility parameters given in Table 2, and 20 trajectories (red curves) of peak timing obtained by aleatoric variation (19), (20) of these parameters with the indicated values of ε. The transmission parameters $\boldsymbol{\beta}$ always have the values (16).

alternative results for the peak timing of Scenario 1 obtained for aleatoric variations (19), (20) of $\boldsymbol{m}^*$ (based on $\boldsymbol{m}$ and $\boldsymbol{m}_{\mathrm{h}}$ given by (17), (18)) with four different values of ε. Figure 8 shows the corresponding results for Scenario 2, where the aleatoric variations are applied to $\boldsymbol{m}^*$ as defined by Table 2.

In Figures 7 and 8, no aleatoric variations are applied to the parameters $\boldsymbol{\beta}$, which are given by (16). To study the sensitivity of the results of peak timing with respect to these parameters, we now keep the mobility parameters constant (namely we employ $\boldsymbol{m}^*$ as given by (17) and (18) for Scenario 1) but apply aleatoric variation to the vector $\boldsymbol{\beta}$ defined by $\tilde{\boldsymbol{\beta}} = (\boldsymbol{\mathcal{I}}_n + \varepsilon\,\mathrm{diag}(\theta_1, \ldots, \theta_n))\boldsymbol{\beta}$. Figures 9 (a), (c) and (e) show the variation in peak timing as produced by aleatoric variations to $\boldsymbol{\beta}$ as given by (16), while Figures 9 (b), (d) and (f) show corresponding results for the choice $\boldsymbol{\beta} = \gamma \boldsymbol{e}$, which corresponds to $\mathcal{R}_{0,j} = 1$ for $j = 1, \ldots, n$.

We observe that the peak timing curves for Scenario 1 and 2 without aleatoric variation of the mobility parameters (the blue curves in the plots of Figures 7 and 8, respectively), are quite similar; both indicate that peak times occur first in the southern and then in the northern regions. Moreover, the aleatoric variations produce curves (drawn in red in Figures 7 and 8) that stay fairly close to those produced by using the original mobility parameters, but where the width of the

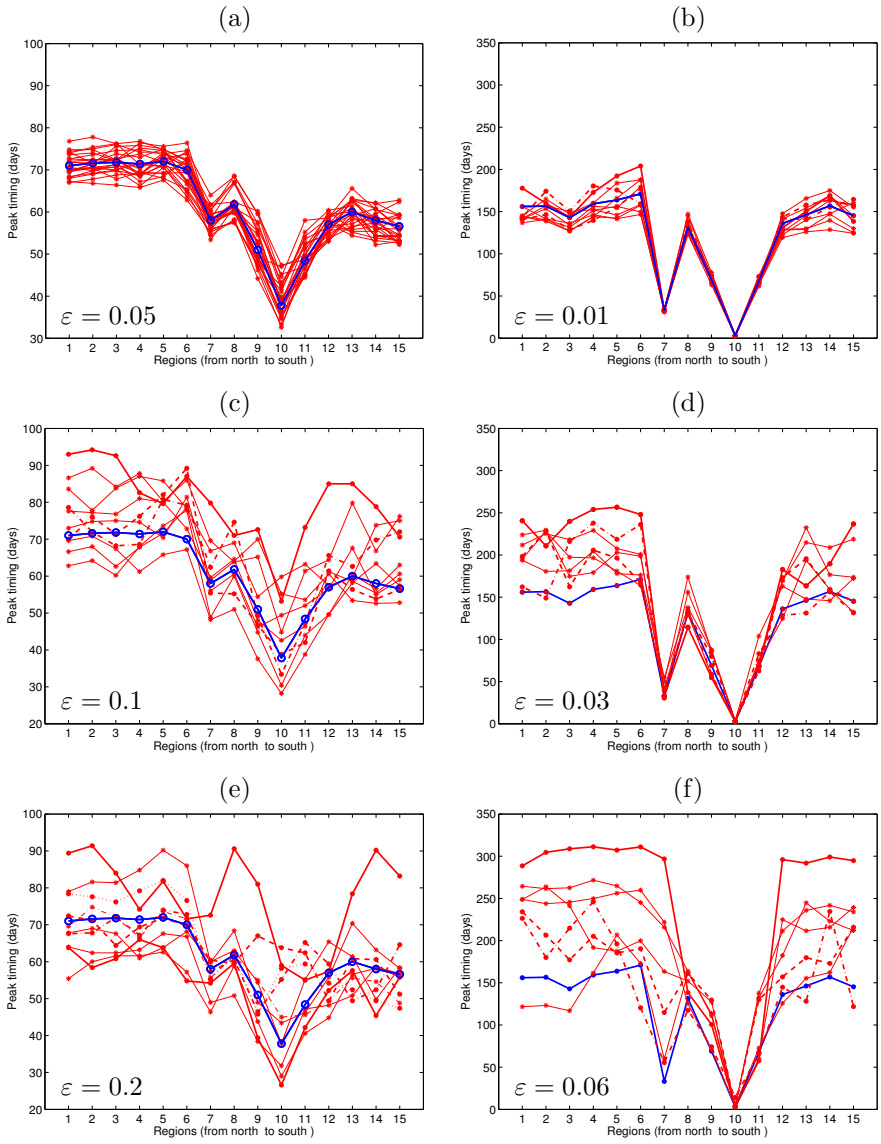

FIGURE 9. Peak timing for Scenario 1 for mobility parameters (17), (18). The blue curves correspond to the fixed choice of $\boldsymbol{\beta}$ given by (a, c, e) (16), (b, d, f) $\boldsymbol{\beta} = \gamma \boldsymbol{e}$. The (a) 20, (b–f) 10 red curves correspond to peak timings obtained under aleatoric variation of $\boldsymbol{\beta}$ with the indicated values of ε.

neighborhood that contains the curves obtained by aleatoric variation increases with ε. All of the red curves still roughly reproduce the north-south gradient in peak timing. These results (obtained under variation of $\boldsymbol{m}^*$ with $\boldsymbol{\beta}$ fixed) contrast with those of Figure 9, obtained under variation of $\boldsymbol{\beta}$ keeping $\boldsymbol{m}^*$ fixed. It turns out that only slight variations of $\boldsymbol{\beta}$ produce significant variations in the pattern of peak timing. These results seem to indicate that the results are less sensitive to variations

in the mobility parameters than to variations in the transmission coefficients in each region.

6. **Conclusions and discussion.** We have used epidemic modeling to gain a better understanding of the underlying mechanisms that shaped the spatial-temporal progression of the 2009 A/H1N1 influenza pandemic in Chile. Our results show that a relatively simple spatial SEIR transmission model that incorporates two key features namely: 1) heterogeneity in local transmission rates previously estimated to be associated with local environmental conditions [12] and 2) population mixing modeled through people's mobility to regions nearby and all other regions via a "hub region" corresponding to the metropolitan central region in Chile (Figure 1 (c)) is able to reproduce broad features of the spatial and temporal pattern of the 2009 pandemic in Chile (Figure 2). These results further support that our SEIR metapopulation model provides a suitable basic framework to describe the 2009 A/H1N1 influenza pandemic at the regional level; see e.g., [38]. Moreover, our findings suggest that the south-north gradient in pandemic peak timing observed in Chile in 2009 is consistent with the pandemic virus starting local transmission in central or southern regions of Chile while it is unlikely that the pandemic started in northern regions (Figure 2). Indeed our findings are in line with a retrospective study based on emergency room visits and laboratory viral surveillance conducted in the southern city of Puerto Montt, capital of Los Lagos region, suggesting that this region could have experienced both earlier pandemic onset and a faster transmission rate compared to the metropolitan area of Santiago [37]. Importantly, our results suggest that our relatively simple modeling framework provides a useful basis to model spatial-temporal spread of pandemic influenza. Moreover, our results suggest that future influenza pandemics are likely to roughly follow a similar south-north gradient in peak timing with southern regions experiencing earlier pandemic peak than northern regions. Hence, our findings may inform pandemic preparedness and control of pandemic influenza. In this context we comment that the progression of peak timing is not an obvious consequence of (2) since 1) population size across regions varies substantially (see Table 1) and hence rates of susceptible depletion are not equal across areas, 2) the local transmission rate is influenced by movement of individuals not only from neighboring areas but also from the hub region and 3) the presence of a hub region (metropolitan area) that connects all regions of Chile plays a role of an homogenizer of transmission dynamics, which does not make obvious the result of a gradient in peak timing that matches the actual data, and 4) initial conditions also matter, as shown in Figure 3.

Our results also indicate that the hub region in our metapopulation model that corresponds to the metropolitan region of Chile plays the critical role of enhancing population mixing across regions in a relatively short period of time (see also [22, 24]). Hence, in our model the pandemic virus quickly spreads across the entire territory soon after the initial cases are seeded in any region of the country. Overall, the peak timing tended to occur first in the region where the initial cases were first introduced, but it then rapidly spread throughout the country and was locally modulated by the corresponding transmissibility level as measured by the local $\mathcal{R}_0$ in each region, which followed a decreasing trend from the southernmost to the northernmost regions of Chile. In contrast to the transmission model with hub, our transmission model with only spatial local diffusion was not able to generate realistic pandemic profiles that were qualitatively consistent with the

2009 A/H1N1 pandemic data from Chile. Not surprisingly, the spatial model with nearest-neighbor diffusion alone generated the best fits to peak timing data when the initial cases were introduced in the southernmost regions of Chile (not shown), but it would require unrealistically high levels of population mobility to neighboring regions.

It is interesting to note that the south-north spreading wave of 2009 pandemic activity in Chile is reminiscent of the spread of the 2009 pandemic in Brazil, with the southernmost regions of this country being hit earlier and experiencing greater severity than northern regions [42]. This suggests that our transmission model with a hub represented by the highly connected areas of the south of Brazil (e.g., São Paulo, Rio do Janeiro) and a similar south-north gradient in transmissibility could be able to generate a qualitatively similar pattern to that observed in 2009 in that country. By contrast, seasonal influenza has been observed to originate from low-population regions in the equatorial north of Brazil and travel to highly populous regions in the subtropical south over a 3-month period [2], together with a weak transmissibility gradient [14].

Although we have focused on characterizing the pandemic peak timing of the spreading wave of 2009 A/H1N1 influenza, the timing of pandemic onset could not be well characterized using our dataset comprising severe acute respiratory infections (SARI), which capture the most severe cases of the severity pyramid. As previously reported [12], the metropolitan region experienced early introductions of the A/H1N1 influenza virus in May 2009, but local outbreaks did not immediately follow, which suggests that local climatic conditions at the time did not enable widespread transmission in the region. Instead, epidemiological investigations revealed that the well-connected southern city of Puerto Montt experienced full-scale transmission of novel A/H1N1 influenza as of late April 2009 before the confirmation of the first case in the country [37].

It is worth noting that we did not attempt to quantify the exact magnitude and progression of the spread of the 2009 A/H1N1 influenza pandemic because our SARI data for Chile only allowed the approximate identification of the timing of evolution of the pandemic (e.g. peak timing) across regions rather than a more accurate assessment of pandemic burden over time and across regions. Furthermore, the quantification of the magnitude of the pandemic in terms of attack rates would probably not only require further data (e.g, serological studies) but also more complex models than those employed here. For instance, we did not model the effect of winter vacation periods on transmission rates although the winter school break in 2009 took place after the pandemic had already reached peak levels across most parts of the country [12]. In addition, we did not account for the high antiviral use rates that characterized Chile, a country where treatment with oseltamivir was recommended for all symptomatic individuals with influenza that were 5 years of age and older [37]. In fact, although treatment of oseltamivir (Tamiflu) has been shown reduce influenza-related mortality in retrospective studies (e.g., [10]), its effect on reducing illness/infectiousness is debated as recently pointed out in a systematic review by Jefferson et al. [27]. Even more importantly, because less than 0.01% of those that got infected with 2009 A/H1N1 influenza succumbed to the disease (see e.g., [45]), its impact on the transmission dynamics of influenza at the population level is negligible. Hence, we do not explicitly model the impact of oseltamivir on influenza mortality in our study. Moreover, assessing the benefits of Tamiflu on the morbidity and mortality burden of influenza is beyond the scope of this study.

It is worth noting that assuming constant rather than time-dependent mobility rates via parameters m and m_{h} was sufficient to capture the region-specific epidemiological course of the pandemic. This may be explained by the fact that it was clear that the A/H1N1 pandemic virus was associated with very low rates of severe disease and death by the time that the first cases of the novel virus were reported in Chile in early May 2009.

Our findings that the pandemic likely took off from southern regions is in line with a retrospective study based on emergency room visits and laboratory viral surveillance conducted in the southern city of Puerto Montt, capital of Los Lagos region [37]. Our findings could have important implications for pandemic preparedness as our results suggest that future influenza pandemics are likely to follow a similar spatial temporal pattern to that of the 2009 A/H1N1 influenza pandemic. This results suggest intensified surveillance strategies in southern regions for the prompt detection of novel influenza viruses.

Acknowledgments. RB is supported by Fondecyt project 1130154; Conicyt project Anillo ACT1118 (ANANUM); Red Doctoral REDOC.CTA, MINEDUC project UCO1202 at Universidad de Concepción; BASAL project CMM, Universidad de Chile and Centro de Investigación en Ingeniería Matemática (CI^{2}MA), Universidad de Concepción; and Centro CRHIAM Proyecto Conicyt Fondap 15130015. PM is supported by Spanish MINECO projects MTM2011-22741 and MTM2014-54388-P. LMV is supported by Fondecyt project 11140708.

REFERENCES

[1] L. J. S. Allen, B. M. Bolker, Y. Lou and A. L. Nevai, Asymptotic of the steady states for an SIS epidemic patch model, *SIAM J. Appl. Math.*, **67** (2007), 1283–1309.

[2] W. J. Alonso, C. Viboud, L. Simonsen, E. W. Hirano, L. Z. Daufenbach and M. A. Miller, Seasonality of influenza in Brazil: A traveling wave from the Amazon to the subtropics, *Amer. J. Epidemiol.*, **165** (2007), 1434–1442.

[3] R. M. Anderson and R. M. May, *Infectious Diseases of Humans: Dynamics and Control*, Oxford Science Publications, 1991.

[4] J. Arino, Diseases in metapopulations. In Z. Ma, Y. Zhou and J. Wu (Eds.), *Modeling and Dynamics of Infectious Diseases, Higher Education Press,* Beijing, **11** (2009), 64–122.

[5] J. Arino, J. R. Davis, D. Hartley, R. Jordan, J. M. Miller and P. van den Driessche, A multi-species epidemic model with spatial dynamics, *Mathematical Medicine and Biology*, **22** (2005), 129–142.

[6] J. Arino and P. van den Driessche, A multi-city epidemic model, *Math. Popul. Studies*, **10** (2003), 175–193.

[7] D. Balcan, H. Hu, B. Goncalves, P. Bajardi, C. Poletto, J. J. Ramasco, D. Paolotti, N. Perra, M. Tizzoni, W. Van den Broeck, V. Colizza and A. Vespignani, Seasonal transmission potential and activity peaks of the new influenza A(H1N1): A Monte Carlo likelihood analysis based on human mobility, *BMC Med.*, **7** (2009), p45 (12pp).

[8] F. Brauer and C. Castillo-Chavez, *Mathematical Models in Population Biology and Epidemiology*, Second Ed., Springer, New York, 2012.

[9] S. Cauchemez, N. Ferguson, C. Wachtel, A. Tegnell, G. Saour, B. Duncan and A. Nicoll, Closure of schools during an influenza pandemic, *Lancet Infect. Dis.*, **9** (2009), 473–481.

[10] G. Chowell, S. Echevarría-Zuno, C. Viboud, L. Simonsen, M. A. Miller, I. Fernández-Gárate, C. González-Bonilla and V. H. Borja-Aburto, Epidemiological characteristics and underlying risk factors for mortality during the autumn 2009 pandemic wave in Mexico, *PLoS One*, **7** (2012), e41069 (10pp).

[11] G. Chowell, S. Echevarría-Zuno, C. Viboud, L. Simonsen, J. Tamerius, M. A. Miller and V. H. Borja-Aburto, Characterizing the epidemiology of the 2009 influenza A/H1N1 pandemic in Mexico, *PloS Med.*, **8** (2011), e1000436 (13pp).

[12] G. Chowell, S. Towers, C. Viboud, R. Fuentes, V. Sotomayor, L. Simonsen, M. Miller, M. Lima, C. Villarroel and M. Chiu, The influence of climatic conditions on the transmission dynamics of the 2009 A/H1N1 influenza pandemic in Chile, *BMC Infect. Dis.*, **12** (2012), p298 (12pp).

[13] G. Chowell, C. Viboud, C. V. Munayco, J. Gomez, L. Simonsen, M. A. Miller, J. Tamerius, V. Fiestas, E. S. Halsey and V. A. Laguna-Torres, Spatial and temporal characteristics of the 2009 A/H1N1 influenza pandemic in Peru, *PLoS One*, **6** (2011), e21287 (10pp).

[14] G. Chowell, C. Viboud, L. Simonsen, M. Miller and W. J. Alonso, The reproduction number of seasonal influenza epidemics in Brazil, 1996–2006, *Proc. Biol. Sci.*, **277** (2010), 1857–1866.

[15] V. Colizza, A. Barrat, M. Barthelemy, A. J. Valleron and A. Vespignani, Modeling the worldwide spread of pandemic influenza: Baseline case and containment interventions, *PLoS Med.*, **4** (2007), e13 (16pp).

[16] O. Diekmann, H. Heesterbeek and T. Britton, *Mathematical Tools for Understanding Infectious Disease Dynamics*, Princeton Series in Theoretical and Computational Biology, Princeton University Press, 2013.

[17] O. Diekmann, J. A. P. Heesterbeek and J. A. J. Metz, On the definition and the computation of the basic reproduction ratio R_0 in models for infectious diseases in heterogeneous populations, *J. Math. Biol.*, **28** (1990), 365–382.

[18] P. van den Driessche, Deterministic compartmental models: Extensions of basic models, In *F. Brauer, P. van den Driessche and J. Wu (Eds.), Mathematical Epidemiology,* Springer-Verlag, Berlin, **1945** (2008), 147–157.

[19] P. van den Driessche, Spatial structure: Patch models. In *F. Brauer, P. van den Driessche and J. Wu (Eds.), Mathematical Epidemiology,* Springer-Verlag, Berlin, **1945** (2008), 179–189.

[20] P. van den Driessche, L. Wang and X. Zou, Impact of group mixing on disease dynamics, *Math. Biosci.*, **228** (2010), 71–77.

[21] P. van den Driessche and J. Watmough, Reproduction numbers and sub-threshold endemic equilibria for compartmental models of disease transmission, *Math. Biosci.*, **180** (2002), 29–48.

[22] X. Fei, C. Connell McCluskey and R. Cressman, Spatial spread of an epidemic through public transportation systems with a hub, *Math. Biosci.*, **246** (2013), 164–175.

[23] J. R. Gog, S. Ballesteros, C. Viboud, L. Simonsen, O. N. Bjornstad, J. Shaman, D. L. Chao, F. Khan and B. T. Grenfell, Spatial transmission of 2009 pandemic influenza in the US, *PLoS Comput. Biol.*, **10** (2014), e1003635 (11pp).

[24] M. Herrera-Valdez, M. Cruz-Aponte and C. Castillo-Chavez, Multiple outbreaks for the same pandemic: Local transportation and social distancing explain the different waves of A-H1N1pdm cases observed in México during 2009, *Math. Biosci. Eng.*, **8** (2011), 21–48.

[25] Instituto Nacional de Estadísticas (INE). Estadísticas Demográficas y Vitales, 2009. Available from: `http://www.ine.cl/canales/chile_estadistico/demografia_y_vitales/demo_y_vita.php`

[26] C. Jackson, E. Vynnycky, J. Hawker, B. Olowokure and P. Mangtani, School closures and influenza: Systematic review of epidemiological studies, *BMJ open*, **3** (2) (2013), e002149 (10pp).

[27] T. Jefferson, M. A. Jones, P. Doshi, C. B. Del Mar, R. Hama, M. J. Thompson, E. A. Spencer, I. Onakpoya, K. R. Mahtani, D. Nunan, J. Howick and C. Heneghan, Neuraminidase inhibitors for preventing and treating influenza in healthy adults and children, *Cochrane Database Syst. Rev.*, April 10, 2014 (560pp).

[28] W. O. Kermack and A. G. McKendrick, A contribution to the mathematical theory of epidemics, *Proc. Roy. Soc. A*, **115** (1927), 700–721.

[29] K. Khan, J. Arino, W. Hu, P. Raposo, J. Sears, F. Calderon, C. Heidebrecht, M. Macdonald, J. Liauw, A. Chan and M. Gardam, Spread of a novel influenza A (H1N1) virus via global airline transportation, *New Engl. J. Med.*, **361** (2009), 212–214.

[30] T. Kuniya, Global stability of a multi-group SVIR epidemic model, *Nonlin. Anal. Real World Appl.*, **14** (2013), 1135–1143.

[31] T. Kuniya, Y. Muroya and Y. Enatsu, Threshold dynamics of an SIR epidemic model with hybrid and multigroup of patch structures, *Math. Biosci. Eng.*, **11** (2014), 1375–1393.

[32] M. Y. Li and Z. Shuai, Global stability of an epidemic model in a patchy environment, *Canad. Appl. Math. Quart.*, **17** (2009), 175–187.

[33] A. Lowen, S. Mubareka, J. Steel and P. Palese, Influenza virus transmission is dependent on relative humidity and temperature, *PLoS Pathog.*, **3** (2007), 1470–1476.

[34] A. Lowen, J. Steel, S. Mubareka and P. Palese, High temperature (30 degrees C) blocks aerosol but not contact transmission of influenza virus, *J. Virol.*., **82** (2008), 5650–5652.
[35] S. Mubareka, A. Lowen, J. Steel, A. Coates, A. Garcia-Sastre and P. Palese, Transmission of influenza virus via aerosols and fomites in the guinea pig model, *J. Infect. Dis.*, **199** (2009), 858–865.
[36] L. Opatowski, C. Fraser, J. Griffin, E. de Silva, M. D. Van Kerkhove, E. J. Lyons, S. Cauchemez and N. M. Ferguson, Transmission characteristics of the 2009 H1N1 influenza pandemic: Comparison of 8 Southern hemisphere countries, *PLoS Pathog.* **7** (2011), e1002225 (10pp).
[37] E. Pedroni, M. Garcia, V. Espinola, A. Guerrero, C. Gonzalez, A. Olea, M. Calvo, B. Martorell, M. Winkler and M. Carrasco, Outbreak of 2009 pandemic influenza A/H1N1, Los Lagos, Chile, April–June 2009, *Eurosurveillance* **15** (2010), 19456 (9pp).
[38] M. M. Saito, S. Imoto, R. Yamaguchi, H. Sato, H. Nakada, M. Kami, S. Miyano and T. Higuchi, Extension and verification of the SEIR model on the 2009 influenza A (H1N1) pandemic in Japan, *Math. Biosci.*, **246** (2013), 47–54.
[39] L. Sattenspiel, *The Geographic Spread of Infectious Diseases: Models and Applications, Princeton Series in Theoretical and Computational Biology*, Princeton University Press, 2009.
[40] L. Sattenspiel and K. Dietz, A structured epidemic model incorporating geographic mobility among regions, *Math. Biosci.*, **128** (1995), 71–91.
[41] D. L. Schanzer, J. M. Langley, T. Dummer and S. Aziz, The geographic synchrony of seasonal influenza: A waves across Canada and the United States, *PLoS One*, **6** (2011), e21471 (8pp).
[42] C. Schuck-Paim, C. Viboud, L. Simonsen, M. A. Miller, F. E. Moura, R. M. Fernandes, M. L. Carvalho and W. J. Alonso, Were equatorial regions less affected by the 2009 influenza pandemic? The Brazilian experience, *PLoS One*, **7** (2012), e41918 (10pp).
[43] J. Shaman and M. Kohn, Absolute humidity modulates influenza survival, transmission, and seasonality, *Proc. Natl. Acad. Sci. USA*, **106** (2009), 3243–3248.
[44] J. Shaman, V. Pitzer, C. Viboud, B. Grenfell and M. Lipsitch, Absolute humidity and the seasonal onset of influenza in the continental United States, *PLoS Biol.,* **8** (2010), e1000316 (13pp).
[45] L. Simonsen, P. Spreeuwenberg, R. Lustig, R. J. Taylor, D. M. Fleming, M. Kroneman, M. D. Van Kerkhove, A. W. Mounts, W. J. Paget and GLaMOR Collaborating Teams, Global mortality estimates for the 2009 Influenza Pandemic from the GLaMOR project: a modeling study, *PLoS Med.*, **10** (2013), e1001558 (17pp).
[46] J. Steel, P. Palese and A. Lowen, Transmission of a 2009 pandemic influenza virus shows a sensitivity to temperature and humidity similar to that of an H3N2 seasonal strain, *J. Virol.*, **85** (2011), 1400–1402.
[47] R. Sun, Global stability of the endemic equilibrium of multigroup SIR models with nonlinear incidence, *Comput. Math. Applic.*, **60** (2010), 2286–2291.
[48] J. Tamerius, M. I. Nelson, S. Z. Zhou, C. Viboud, M. A. Miller and W. J. Alonso, Global influenza seasonality: Reconciling patterns across temperate and tropical regions, *Environ. Health Perspect.*, **119** (2011), 439–445.
[49] C. Viboud, O. N. Bjornstad, D. L. Smith, L. Simonsen, M. A. Miller and B. T. Grenfell, Synchrony, waves, and spatial hierarchies in the spread of influenza, *Science*, **312** (2006), 447–451.
[50] E. Vynnycky and R. E. White, *An Introduction to Infectious Disease Modelling*, Oxford University Press, 2010.
[51] J. B. Wenger and E. N. Naumova, Seasonal synchronization of influenza in the United States older adult population, *PLoS One*, **5** (2010), e10187 (11pp).
[52] H. Yu, S. Cauchemez, C. A. Donnelly, L. Zhou, L. Feng, N. Xiang, J. Zheng, M. Ye, Y. Huai, Q. Liao, Z. Peng, Y. Feng, H. Jiang, W. Yang, Y. Wang, N. M. Ferguson and Z. Feng, Transmission dynamics, border entry screening, and school holidays during the 2009 influenza A (H1N1) pandemic, China, *Emerg. Infect. Dis.*, **18** (2012), 758–766.

Received July 21, 2014; Accepted July 10, 2015.

E-mail address: rburger@ing-mat.udec.cl
E-mail address: gchowell@gsu.edu
E-mail address: mulet@uv.es
E-mail address: lvillada@ubiobio.cl